

RESEARCH ARTICLE | SEPTEMBER 30 2021

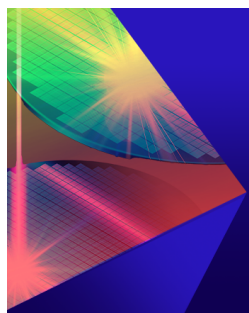
Three-dimensional vortex characterization in small intracranial aneurysms based on four dimensional flow magnetic resonance imaging at 7 Tesla

Ang Zhou ; Bharathi D. Jagadeesan ; Sean L. Moen ; Andrew W. Grande ; Pierre-Francois Van de Moortele 




AIP Advances 11, 095022 (2021)

<https://doi.org/10.1063/5.0066250>



AIP Advances
Special Topic: Novel Applications of Focused Ion Beams — Beyond Milling
Submit Today



Three-dimensional vortex characterization in small intracranial aneurysms based on four dimensional flow magnetic resonance imaging at 7 Tesla

Cite as: AIP Advances 11, 095022 (2021); doi: 10.1063/5.0066250

Submitted: 9 August 2021 • Accepted: 8 September 2021 •

Published Online: 30 September 2021



View Online



Export Citation



CrossMark

Ang Zhou,^{1,2,a)}  Bharathi D. Jagadeesan,^{3,4,5}  Sean L. Moen,⁴  Andrew W. Grande,^{4,6} 
and Pierre-Francois Van de Moortele¹ 

AFFILIATIONS

¹Center for Magnetic Resonance Research, University of Minnesota, Minneapolis, Minnesota 55455, USA

²Department of Radiology and Biomedical Imaging, University of California San Francisco, San Francisco, California 94143, USA

³Department of Radiology, University of Minnesota, Minneapolis, Minnesota 55455, USA

⁴Department of Neurosurgery, University of Minnesota, Minneapolis, Minnesota 55455, USA

⁵Department of Neurology, University of Minnesota, Minneapolis, Minnesota 55455, USA

⁶Stem Cell Institute, University of Minnesota, Minneapolis, Minnesota 55455, USA

^{a)} Author to whom correspondence should be addressed: zhouang48@gmail.com

ABSTRACT

Effective vectors and approaches are proposed to identify the three-dimensional (3D) vortex motion in small intracranial aneurysms (≤ 7 mm) based on four dimensional flow magnetic resonance imaging at 7 T. Six subjects with small intracranial aneurysms were scanned. The 3D vortex identification vector \vec{T}_2 and scalar Ω are computed with velocity vectors. The high $T_{2,magnitude}$ region is defined using region growing based on the threshold value determined by an empirical nonlinear relation between $T_{2,magnitude}$ and the scalar Ω inside the aneurysmal sac, while the threshold of $\Omega = 0.6$ is used to define the high Ω region. The spatially averaged vector \vec{T}_2 and the vorticity vector $\vec{\omega}$ over the defined high $T_{2,magnitude}$ and Ω regions are found to denote the corresponding vortex motion directions, respectively. With these two vectors, the 3D vector \vec{T}_1 is invoked to localize vortex motion centers. Threshold values of region growing for the high $T_{2,magnitude}$ region from the nonlinear relation for each subject are in the range of 0.51 and 0.59. The volume of the defined high $T_{2,magnitude}$ region is close to that of the defined high Ω region. The angle between the generated two averaged vectors \vec{T}_2 and $\vec{\omega}$ is small for all subjects, with the maximum being 9.17° . The located vortex motion centers from \vec{T}_1 based on \vec{T}_2 and $\Omega(\omega)$ are the same for each subject inside the aneurysm. The small angle between the two averaged vectors and the located same vortex center supports the effectiveness of the proposed method to characterize vortices in small unruptured intracranial aneurysms.

© 2021 Author(s). All article content, except where otherwise noted, is licensed under a Creative Commons Attribution (CC BY) license (<http://creativecommons.org/licenses/by/4.0/>). <https://doi.org/10.1063/5.0066250>

I. INTRODUCTION

Incidentally found small (≤ 7 mm) intracranial aneurysms (SIAs) affect ~ 1 in 50 individuals.¹ Management of patients with this condition poses a unique challenge for neurovascular specialists: while many SIAs ≤ 7 mm remain stable and pose little to no

risk to the patient,^{2,3} some, if left untreated, have the potential to rupture, causing potentially devastating subarachnoid hemorrhage (SAH).⁴⁻⁶ The preemptive treatment (surgical or endovascular) of SIAs, however, carries morbidity and mortality risks,⁷ making universal preventive treatment impractical in the management of the majority of patients with SIAs. A reliable methodology to accurately

quantify the future risk of rupture for individual SIAs is, therefore, of high importance in the management of this disease. Multiple efforts have been made to improve risk stratification by investigating intra-aneurysmal hemodynamic parameters and their role in aneurysm formation, growth, and rupture.^{8–10}

These studies have been predominantly performed using sophisticated computational fluid dynamics (CFD) models,^{11,12} and more recently, non-invasive 4D flow magnetic resonance imaging (4D Flow MRI) techniques have revealed the presence of regions with vortical flow within IAs. They have also shown that the region(s) with vortical blood flow is always organized around a dominant and fixed rotational axis.¹³ The majority of studies have reported the presence of vortices in IAs,^{9,14} but some have reported them in a subset of IAs with some other different inflow jet patterns.^{10,15} Regardless, it is possible that quantitative measures of vortical flows could yield information that can be useful in risk stratification of aneurysm rupture. However, the dynamic nature of these structures has made them somewhat difficult to unambiguously define¹⁶ and analyze. To date, the identification and classification of IA vortices have largely relied on two representations: either a vorticity contour along with velocity vectors evaluated on an arbitrarily defined two dimensional plane¹⁷ across the vortex or a 3D vortex core region containing velocity streamline bundles with values below a certain threshold.¹⁴ Neither of these techniques has enabled a deeper understanding of the various components of vortical flow such as fluid particle deformation, pure rotational flow, and tangential shear, all of which could have physiological significance. For instance, fluid particle deformation in blood could result in mechanical stresses to blood cells, resulting in activation of inflammatory or thrombogenic pathways.^{18,19} Likewise, rotational flow could affect the transit time of blood cells within aneurysms. In this article, we describe a novel three-dimensional methodology that could be used to distinguish between the fluid particle deformation and rotational components of vortices within SIAs when it is used in conjunction with a previously proposed 3D technique.

We demonstrate the utilization of our methodology through the study of intra-aneurysmal vortices that were detected in a small series of SIAs that were imaged on a 7 T MRI system using the 4D Flow technique.

II. METHODS

A. Subjects

Following informed consent, participants with IA were enrolled in a prospective Health Insurance Portability and Accountability Act (HIPAA) compliant study approved by our institutional review board (clinicaltrials.gov NCT02576743). Inclusion criteria included the following: patient presentation with an unruptured intracranial aneurysm measuring ≤ 7 mm in its largest dimension on standard of care clinical imaging with Computed Tomography (CT) or catheter angiography. Exclusion criteria included all the contraindications to ultra-high field MRI, history of aneurysm rupture, aneurysms measuring >7 mm, presence of cerebrovascular disorders such as atherosclerosis or vascular malformations, cardiac failure or cardiac arrhythmias, which preclude electrocardiogram (ECG) gating, pre-existing significant neurological deficits from ischemic stroke or intracranial hemorrhage, and pregnancy. A total of six patient datasets were included in this study, and informed consent was obtained from all six subjects.

B. 4D Flow MRI acquisition and analysis

All 6 patients [5 females and 1 male, average age (SD) = 58 ± 14 years] were scanned on a 7 T whole body scanner (Magnetom, Siemens, Erlangen, Germany) equipped with a 32-channel head coil (NovaMedical, Wilmington, MA). A cardiac-gated (three lead ECG), 4-point 3-directional 4D Flow sequence was used to image an axial oblique 3D slab centered on the aneurysm. The relevant parameters are as follows: 2 or 3 k-space lines per cardiac phase, spatial resolution of $(0.62\text{--}0.76) \times (0.65\text{--}0.76) \times (0.6\text{--}0.8)$ mm³ (before interpolation), TR/TE = 6.2–6.5/3.29–3.53 ms, temporal resolution of 49.6–78 ms, number of phases per cardiac cycle between 10 and 15, and Generalized Autocalibrating Partially Parallel Acquisitions (GRAPPA) factor of $\times 2$ in one subject and $\times 3$ in five subjects. Encoding velocity (VENC) was set to 0.8 or 1.0 m/s (the same value applied along x, y, and z axes). Subjects' demographics and relevant magnetic resonance imaging (MRI) acquisition parameters are shown in Table I.

Magnitude and phase difference 4D Flow Digital Imaging and Communications in Medicine (DICOM) images were imported to a desktop personal computer (PC) and preprocessed using VeloMap²⁰

TABLE I. Summary of scan information of subjects. The size (column 5) indicates the three dimensions of the aneurysm (longest to shortest).

Subjects	Age	Gender	Aneurysm location	Size (mm)	TE/TR (ms)	Encoding velocity (m/s)	Acquisition resolution (mm)
S1	46	Female	Left superior hypophyseal artery	$\approx 4.9 \times 4.8 \times 3.9$	3.38/6.3	$0.8 \times 0.8 \times 0.8$	$0.76 \times 0.76 \times 0.8$
S2	63	Male	Right pericallosal artery	$\approx 6.1 \times 5.9 \times 3.6$	3.29/6.2	$0.8 \times 0.8 \times 0.8$	$0.76 \times 0.76 \times 0.8$
S3	78	Female	Right ventral superior hypophyseal artery	$\approx 3.9 \times 3.8 \times 3.7$	3.29/6.2	$0.8 \times 0.8 \times 0.8$	$0.76 \times 0.76 \times 0.8$ ^a ($0.38 \times 0.38 \times 0.40$)
S4	63	Female	Right internal carotid artery	$\approx 2.1 \times 2.0 \times 1.3$	3.53/6.5	$1.0 \times 1.0 \times 1.0$	$0.62 \times 0.68 \times 0.6$ ^a ($0.31 \times 0.31 \times 0.30$)
S5	60	Female	Ophthalmic segment of left internal carotid artery	$\approx 2.4 \times 2.0 \times 1.7$	3.53/6.5	$1.0 \times 1.0 \times 1.0$	$0.62 \times 0.68 \times 0.6$ ^a ($0.31 \times 0.31 \times 0.30$)
S6	38	Female	Ophthalmic segment of right internal carotid artery	$\approx 4.2 \times 3.2 \times 2.8$	3.48/6.5	$1.0 \times 1.0 \times 1.0$	$0.65 \times 0.65 \times 0.6$ ^a ($0.33 \times 0.33 \times 0.30$)

^aColumn 8: for subjects S3, S4, S5, and S6, data were interpolated ($\times 2$) during image reconstruction on the MR console in the three axes.

in Matlab (MathWorks, Natick, MA) for noise reduction, velocity unwrapping, and eddy current correction. A 3D phase contrast magnetic resonance angiogram (PC-MRA) was generated by combining magnitude and phase images in VeloMap. The data were then imported into Mimics and 3-Matic (Materialize, Leuven, Belgium) to manually generate 3D masks that included the aneurysm and its parent artery. The velocity vectors in the aneurysm and its parent artery(ies) were generated by VeloMap.

Throughout the current study, velocity vectors of all cardiac phases were averaged together prior to the vortex analysis in order to maximize the signal to noise ratio.

C. Vortex identification methods

1. $\vec{\Gamma}_1$ and $\vec{\Gamma}_2$ based method

Several flow features have been reported in vortices, including rotational flow and shear flow. Γ_2 is a dimensionless scalar that has been previously used to identify the vortical flow region dominated by rotational flow over shear flow. It is computed at each point within an arbitrarily defined two dimensional flow plane that intersects a given vortex.²¹ Γ_1 is another dimensionless scalar that has been previously used to identify the center of vortex motion in the same plane.²¹

However, an important limitation of Γ_1 and Γ_2 measurement is their reliance on a manually defined, arbitrarily selected 2D reference vortex intersection plane (2D-VIP). In order to overcome the inevitable biases that can be introduced from this approach, we extended the Γ_1 and Γ_2 formalisms and calculated two corresponding vectors $\vec{\Gamma}_1$ and $\vec{\Gamma}_2$, both of which are defined in the entire 3D volume that encompasses the given vortex rather than on an arbitrary plane.

In a three-dimensional flow domain, the velocity field is first sampled at discrete spatial points, and the constituent three-dimensional velocity vectors are determined at each point P. $\vec{\Gamma}_2$ is then defined as

$$\vec{\Gamma}_2(P) = \frac{1}{N} \sum_{i=1}^N \frac{[\vec{PM}_i \times (\vec{U}_{M_i} - \vec{U}_P)]}{\|\vec{PM}_i\| \cdot \|\vec{U}_{M_i} - \vec{U}_P\|}, \quad (1)$$

where M_i are the $N = 26$ spatial points surrounding the center point P in each cube of $3 \times 3 \times 3 = 27$ voxels and \vec{U}_{M_i} is the velocity vector at each M_i . The local convection velocity vector $\vec{U}_P = \frac{1}{N} \sum_{i=1}^N \vec{U}_{M_i}$ is the velocity vector calculated from the spatial average over these points. \vec{PM}_i is the spatial vector pointing from P to M_i .

$\vec{\Gamma}_2$, therefore, represents the ratio of the rotational flow to shear flow in the vicinity of P and thus provides a way to quantify the rotational direction of the vortex motion at this point. The magnitude of $\vec{\Gamma}_2$ is the square root of the sum of square of its three components. $\Gamma_{2,magnitude}$ is bounded by a maximum value of 1. Strong rotational flow regions are characterized by a high $\Gamma_{2,magnitude}$, which is usually above 0.5.²¹

Similar to $\vec{\Gamma}_2$ but without local convection velocity, $\vec{\Gamma}_1$ is defined as

$$\vec{\Gamma}_1(P) = \frac{1}{N} \sum_{i=1}^N \frac{[\vec{PM}_i \times \vec{U}_{M_i}]}{\|\vec{PM}_i\| \cdot \|\vec{U}_{M_i}\|}. \quad (2)$$

In a three-dimensional flow velocity field, the maximum value for each component of $\vec{\Gamma}_1$ coincides with the center of vortex motion in the 2D plane, which is perpendicular to this component. The absolute value of $\vec{\Gamma}_1$ ranges from 0 – 1.

2. Ω based method

The Ω method, another vortex identification technique that has been proposed by Liu *et al.*,²² is utilized here for comparison with the methodology described above, as well as in combination with the above-mentioned method. Ω has been described as a dimensionless scalar that captures the flow region, in which the vorticity overtakes fluid particle deformation. Vortical flow occurs when there is a local spinning motion of fluid particles around certain points within the flow field. Deformation of fluid particles represents the change in their shape under the effect of applied external forces. Given the velocity field where u , v , and w are the velocity vector components in the x , y , and z directions, respectively, the velocity gradient tensor is composed of two tensors, the strain rate tensor (A) and rotation rate tensor (B),

$$\underbrace{\begin{bmatrix} \frac{\partial u}{\partial x} & \frac{\partial u}{\partial y} & \frac{\partial u}{\partial z} \\ \frac{\partial v}{\partial x} & \frac{\partial v}{\partial y} & \frac{\partial v}{\partial z} \\ \frac{\partial w}{\partial x} & \frac{\partial w}{\partial y} & \frac{\partial w}{\partial z} \end{bmatrix}}_{\text{Velocity Gradient Tensor}} = \frac{1}{2} \underbrace{\begin{bmatrix} 2\frac{\partial u}{\partial x} & \frac{\partial u}{\partial y} + \frac{\partial v}{\partial x} & \frac{\partial u}{\partial z} + \frac{\partial w}{\partial x} \\ \frac{\partial v}{\partial x} + \frac{\partial u}{\partial y} & 2\frac{\partial v}{\partial y} & \frac{\partial v}{\partial z} + \frac{\partial w}{\partial y} \\ \frac{\partial w}{\partial x} + \frac{\partial u}{\partial z} & \frac{\partial w}{\partial y} + \frac{\partial v}{\partial z} & 2\frac{\partial w}{\partial z} \end{bmatrix}}_{\text{Strain Rate Tensor A}} + \frac{1}{2} \underbrace{\begin{bmatrix} 0 & \frac{\partial u}{\partial y} - \frac{\partial v}{\partial x} & \frac{\partial u}{\partial z} - \frac{\partial w}{\partial x} \\ \frac{\partial v}{\partial x} - \frac{\partial u}{\partial y} & 0 & \frac{\partial v}{\partial z} - \frac{\partial w}{\partial y} \\ \frac{\partial w}{\partial x} - \frac{\partial u}{\partial z} & \frac{\partial w}{\partial y} - \frac{\partial v}{\partial z} & 0 \end{bmatrix}}_{\text{Rotation Rate Tensor B}}, \quad (3)$$

where A is symmetric and B is anti-symmetric. The strain rate tensor is constituted by components that depict the rate of change in the deformation of a fluid particle with time, which occurs in the neighborhood of a certain point. The rotation rate tensor consists of vorticity components in the same neighborhood. The square of Frobenius norms for tensors A and B is defined as

$$a = \sum_{i=1}^3 \sum_{j=1}^3 |A_{ij}|^2 = \text{trace}(A^T A), \quad (4)$$

$$b = \sum_{i=1}^3 \sum_{j=1}^3 |B_{ij}|^2 = \text{trace}(B^T B). \quad (5)$$

Ω is defined as the ratio of vorticity squared over the sum of vorticity squared and deformation squared,

$$\Omega = \frac{b}{a + b + \epsilon}, \quad (6)$$

where ϵ is a small parameter allowing us to ensure that the denominator is non-zero. In domains where a and b are close to zero, the impact of noise may become predominant and can be reduced by a small value assigned to ϵ . Empirically, ϵ is evaluated as

$$\epsilon = 0.001(b - a)_{\max}. \quad (7)$$

$(b - a)_{\max}$ represents the maximum difference between the squared vorticity and the squared deformation over the flow domain.²³ The region where vorticity is dominant is typically associated with $\Omega > 0.5$. However, this method has been reported to have a low sensitivity to variations in the Ω threshold within a range of 0.52–0.60.²³ Thus, throughout this study, a threshold of $\Omega = 0.60$ was used to define the high Ω region.

D. Three-dimensional vortex characterization approach utilizing $\vec{\Gamma}_2$ and Ω

- Step 1: $\vec{\Gamma}_2$ and Ω were computed at each spatial point in the three-dimensional flow domain within the aneurysmal sac.
- Step 2: The spatial points inside the aneurysmal sac where $\Gamma_{2,magnitude}$ and Ω attain their maximum values were identified.
- Step 3: The points of maxima for $\Gamma_{2,magnitude}$ and Ω were then used as the initial seed points for a region growing algorithm that defined a high $\Gamma_{2,magnitude}$ and a high Ω region, respectively, within which the values for $\Gamma_{2,magnitude}$ and Ω exceeded a pre-specified threshold. Each of the twenty-six points neighboring the initial seed point was added to the region if and only if its value was greater than or equal to the threshold. The points added to the region were then regarded as new seed points to iterate in the same manner until none of the neighboring points

met the threshold. The high vortex motion region was thereafter defined as a high $\Gamma_{2,magnitude}$ or as a high Ω region, for the $\vec{\Gamma}_2$ -based and the Ω -based methods, respectively.

- Step 4: The spatial averages of the three components of $\vec{\Gamma}_2$, i.e., $\Gamma_{2,x}\vec{i}$, $\Gamma_{2,y}\vec{j}$, and $\Gamma_{2,z}\vec{k}$ (\vec{i} , \vec{j} , and \vec{k} are, respectively, the unit vectors in the x, y, and z directions), were computed over all the spatial points enclosed within the defined high $\Gamma_{2,magnitude}$ region. Similarly, the spatial averages of the three components of vorticity $\vec{\omega} = \omega_x\vec{i} + \omega_y\vec{j} + \omega_z\vec{k}$ were computed over all the spatial points enclosed within the defined high Ω region. Two averaged vectors, $\vec{V}_{\vec{\Gamma}_2}$ and $\vec{V}_{\vec{\omega}}$ (one for $\vec{\Gamma}_2$ and one for $\vec{\omega}$), were then generated over the high $\Gamma_{2,magnitude}$ and high Ω regions, respectively.
- Step 5: Two new orthogonal coordinate systems, $CS_{\vec{\Gamma}_2}$ and $CS_{\vec{\omega}}$, were established. In $CS_{\vec{\Gamma}_2}$, one axis is collinear to $\vec{V}_{\vec{\Gamma}_2}$, while in $CS_{\vec{\omega}}$, one axis is collinear to $\vec{V}_{\vec{\omega}}$. The other two axes were arbitrarily oriented in orthogonal planes that were perpendicular to either $\vec{V}_{\vec{\Gamma}_2}$ or $\vec{V}_{\vec{\omega}}$ and to each other.
- Step 6: Three velocity components at each spatial point were reevaluated in $CS_{\vec{\Gamma}_2}$ and in $CS_{\vec{\omega}}$ through the corresponding coordinate transformations. Three-dimensional $\vec{\Gamma}_{1,\vec{\Gamma}_2}$ and $\vec{\Gamma}_{1,\vec{\omega}}$ vectors was then computed, respectively, based on the transformed velocity vectors in the new coordinate system $CS_{\vec{\Gamma}_2}$ and $CS_{\vec{\omega}}$ for each spatial point inside the aneurysmal sac.
- Step 7: The spatial point inside the aneurysmal sac where the component of $\vec{\Gamma}_{1,\vec{\Gamma}_2}$ collinear to $\vec{V}_{\vec{\Gamma}_2}$ attained its maximum value was

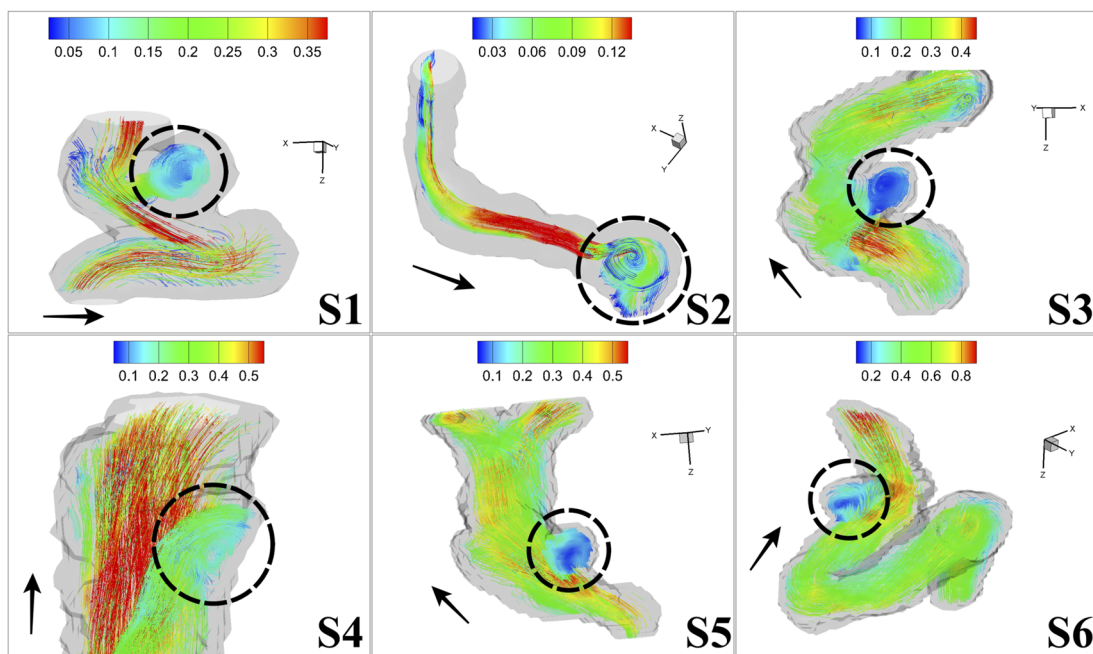


FIG. 1. Cycle averaged original velocity streamline pattern of six subjects showing rotational motion inside aneurysmal sac. Color bars denote the magnitude of velocity. Black dashed circles show the vortex motion inside the aneurysmal sac. Black arrows denote the blood flow directions.

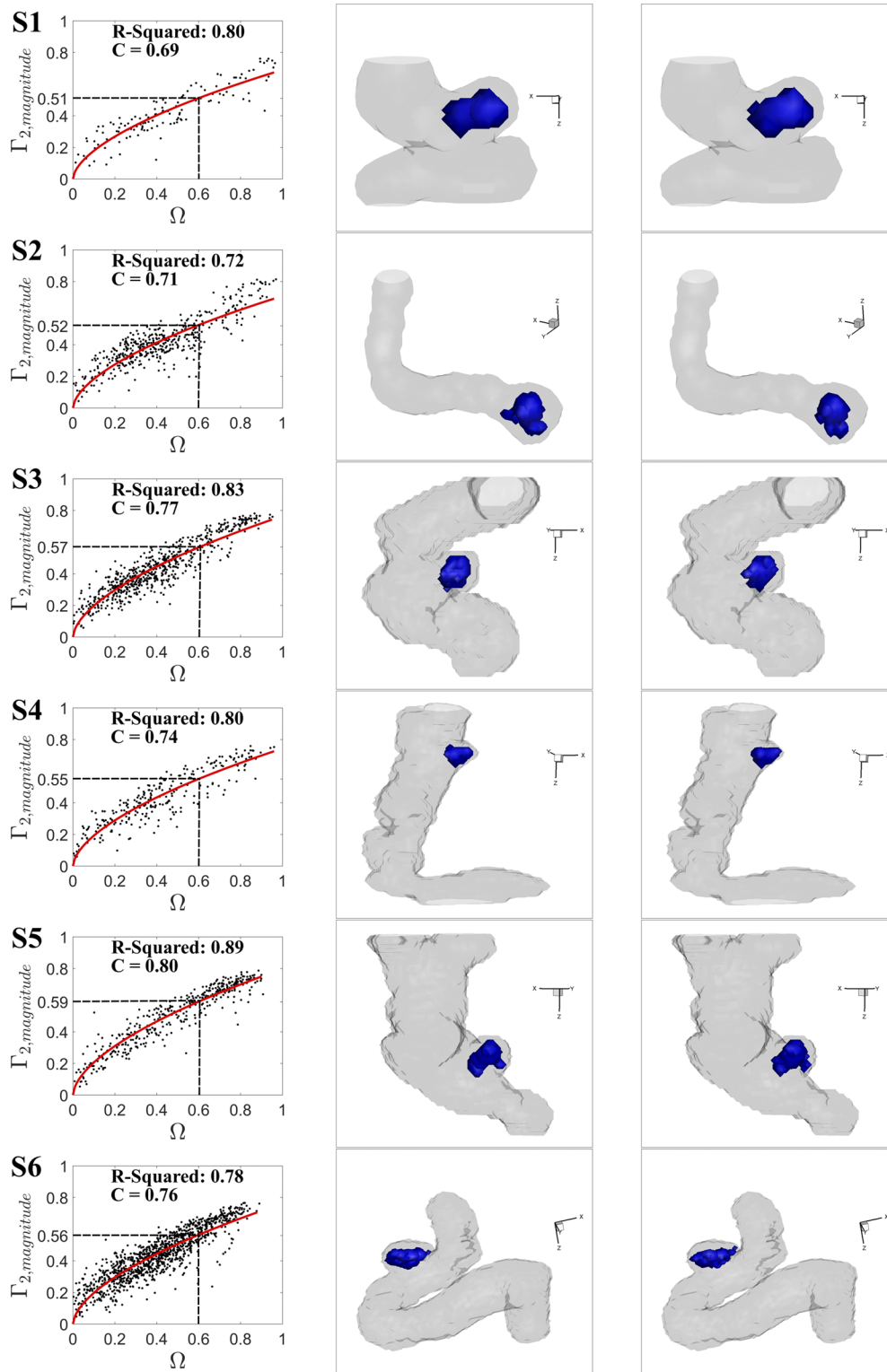


FIG. 2. First column: scatter plot of Ω and $\Gamma_{2,magnitude}$ inside aneurysmal sac with nonlinear regression fit. Red line: $\Gamma_{2,magnitude} = C\Omega^{\frac{1}{1.7}}$. Second column: high $\Gamma_{2,magnitude}$ region (blue) defined by the corresponding threshold of $\Gamma_{2,magnitude}$ to $\Omega = 0.60$. Third column: high Ω region (blue) defined by the threshold of $\Omega = 0.60$.

located and defined as the $\vec{\Gamma}_2$ derived vortex center $C_{\vec{\Gamma}_2}$. A similar operation was performed using $\vec{\Gamma}_{1,\vec{\omega}}$ and $\vec{V}_{\vec{\omega}}$ (instead of $\vec{\Gamma}_{1,\vec{\Gamma}_2}$ and $\vec{V}_{\vec{\Gamma}_2}$) to locate and define the $\vec{\omega}$ derived vortex center $C_{\vec{\omega}}$. A $\vec{V}_{\vec{\Gamma}_2}$ vector and a $\vec{V}_{\vec{\omega}}$ vector were then assigned to each of the points located in $C_{\vec{\Gamma}_2}$ and $C_{\vec{\omega}}$, respectively, based on the respective new coordinate systems to denote the three-dimensional vortex motion directions. The kinetic energy (KE) for flow was defined as half the sum of the three squared components of velocity. The ratio of KE contained within the plane perpendicular to $\vec{V}_{\vec{\Gamma}_2}$ (or to $\vec{V}_{\vec{\omega}}$) to the total KE in the high $\Gamma_{2,magnitude}$ region (or the high Ω region) inside the aneurysmal sac (ratio KE) was also calculated for each approach.

The final results (vortex center, vortex motion direction, magnitude of $\vec{\Gamma}_1$, and ratio KE) obtained with the three-dimensional $\vec{\Gamma}_2$ method were then systematically compared to those obtained with the previously introduced $\Omega(\vec{\omega})$ method.

Computations were conducted in Python and Matlab (MathWorks, Natick, MA), while visualizations were obtained with Tecplot (Bellevue, WA).

E. Results

Figure 1 shows the cycle averaged original velocity streamlines of six subjects. The rotational motion is observed inside the aneurysmal sac for each subject case. The lower threshold of $\Gamma_{2,magnitude}$ utilized to identify the region with high vortex motion was derived in each individual subject from the scatter plot of Ω and $\Gamma_{2,magnitude}$ values inside the corresponding aneurysmal sac (Fig. 2 first column). For each such scatter plot, an empirical nonlinear regression fit, in the form of $\Gamma_{2,magnitude} = C\Omega^{1/7}$, was consistently found between Ω and $\Gamma_{2,magnitude}$ and was used to generate the corresponding threshold of $\Gamma_{2,magnitude}$ based on the 0.60 threshold of Ω . C was found to be very similar for all six aneurysms (mean \pm std, min, max = $0.75 \pm 0.04, 0.69, 0.80$), with R-squared values above 0.7 (mean \pm std, min, max = $0.80 \pm 0.05, 0.72, 0.89$). Although these results indicate that the corresponding value of $\Gamma_{2,magnitude}$ is below that of Ω , it was still consistently distributed above 0.5 in every subject (S1, $\Gamma_{2,magnitude} = 0.51$; S2, $\Gamma_{2,magnitude} = 0.52$; S3, $\Gamma_{2,magnitude} = 0.57$; S4, $\Gamma_{2,magnitude} = 0.55$; S5, $\Gamma_{2,magnitude} = 0.59$; and S6, $\Gamma_{2,magnitude} = 0.56$;

mean \pm std; min, max = $0.55 \pm 0.03, 0.51, 0.59$). The threshold defined high $\Gamma_{2,magnitude}$ and Ω regions are shown in blue on the second and third columns of Fig. 2, respectively. The ratio of the volume of the high $\Gamma_{2,magnitude}$ region to the volume of the defined high Ω region lies around 1 between 0.94 and 1.30 through the subjects (S1, 0.94; S2, 1.04; S3, 1.13; S4, 1.12; S5, 1.01; and S6, 1.30). The dice coefficient of these two regions ranges from 0.76 to 0.90 (S1, 0.83; S2, 0.86; S3, 0.87; S4, 0.81; S5, 0.90; and S6, 0.76). Table II also presents the ratios of the volumes of the defined high $\Gamma_{2,magnitude}$ region and the defined high Ω region to the volume of the aneurysm for each subject. The maximum and mean values of $\Gamma_{2,magnitude}$ within the high $\Gamma_{2,magnitude}$ region as well as the maximum and mean Ω within the high Ω region are presented in Table II. The maximum and mean values of $\Gamma_{2,magnitude}$ are lower than those of Ω in all subjects. However, these maximum and mean values have very limited variations between subjects ($0.76 \leq \max \leq 0.81$ and $0.63 \leq \text{mean} \leq 0.68$). The two vectors $\vec{V}_{\vec{\Gamma}_2}$ and $\vec{V}_{\vec{\omega}}$ are shown for each subject in Fig. 3. In each case, when defining their corresponding anchor points ($C_{\vec{\Gamma}_2}$ and $C_{\vec{\omega}}$)

located by $\vec{\Gamma}_1$, it was found that both vectors shared the same unique anchor point ($C_{\vec{\Gamma}_2} = C_{\vec{\omega}}$). For the purpose of visualization, the mid-points of the two vectors are anchored on the same red diamond label (at the center $C_{\vec{\Gamma}_2} = C_{\vec{\omega}}$) within each aneurysm. The inner angle $\theta_{\vec{\Gamma}_2,\vec{\omega}}$ between these two vectors for each aneurysm is shown in the second column of Table III. The overlapping part of the defined high $\Gamma_{2,magnitude}$ and high Ω regions is used as the region to obtain the voxelwise average for the angle between $\vec{\Gamma}_2$ and $\vec{\omega}$ at each voxel; this averaged angle $\theta_{\vec{\Gamma}_2,\vec{\omega}}$ is shown in the third column in Table III. Table III also presents the ratio of the total kinetic energy contained in the plane perpendicular to either $\vec{V}_{\vec{\Gamma}_2}$ or $\vec{V}_{\vec{\omega}}$ to the total kinetic energy in the corresponding high vortex motion region (either the high $\Gamma_{2,magnitude}$ region or the high Ω region, respectively) within the aneurysmal sac. Figure 4 depicts for each aneurysm a 5×5 isotropic pixel matrix centered on $C_{\vec{\Gamma}_2}$ (first column) or on $C_{\vec{\omega}}$ (second column) in a plane perpendicular to $\vec{V}_{\vec{\Gamma}_2}$ (first column) or to $\vec{V}_{\vec{\omega}}$ (second column). The gray scale shows the magnitude of the component of $\vec{\Gamma}_{1,\vec{\Gamma}_2}$ (first column) or $\vec{\Gamma}_{1,\vec{\omega}}$ (second column) perpendicular to the planes in the same direction as $\vec{V}_{\vec{\Gamma}_2}$ or $\vec{V}_{\vec{\omega}}$. The red arrows show

TABLE II. Second column: ratio of volume of defined high $\Gamma_{2,magnitude}$ region to volume of aneurysm, $RV_{\vec{\Gamma}_2}$. Third column: ratio of volume of defined high Ω region to volume of aneurysm, RV_{Ω} . Fourth column: ratio of $RV_{\vec{\Gamma}_2}$ to RV_{Ω} . Fifth column: maximum and mean $\Gamma_{2,magnitude}$ over the defined high $\Gamma_{2,magnitude}$ region. Sixth column: maximum and mean Ω over the defined high Ω region.

	$RV_{\vec{\Gamma}_2}$	RV_{Ω}	$RV_{\vec{\Gamma}_2}/RV_{\Omega}$	$\Gamma_{2,magnitude}$		Ω	
				Maximum	Mean \pm Std	Maximum	Mean \pm Std
S1	0.27	0.28	0.96	0.76	0.63 ± 0.08	0.96	0.79 ± 0.11
S2	0.18	0.17	1.06	0.81	0.65 ± 0.09	0.97	0.77 ± 0.10
S3	0.21	0.18	1.17	0.78	0.68 ± 0.06	0.95	0.75 ± 0.09
S4	0.24	0.22	1.09	0.76	0.65 ± 0.05	0.96	0.76 ± 0.09
S5	0.42	0.41	1.02	0.79	0.68 ± 0.05	0.91	0.74 ± 0.08
S6	0.21	0.16	1.31	0.77	0.65 ± 0.05	0.89	0.70 ± 0.06

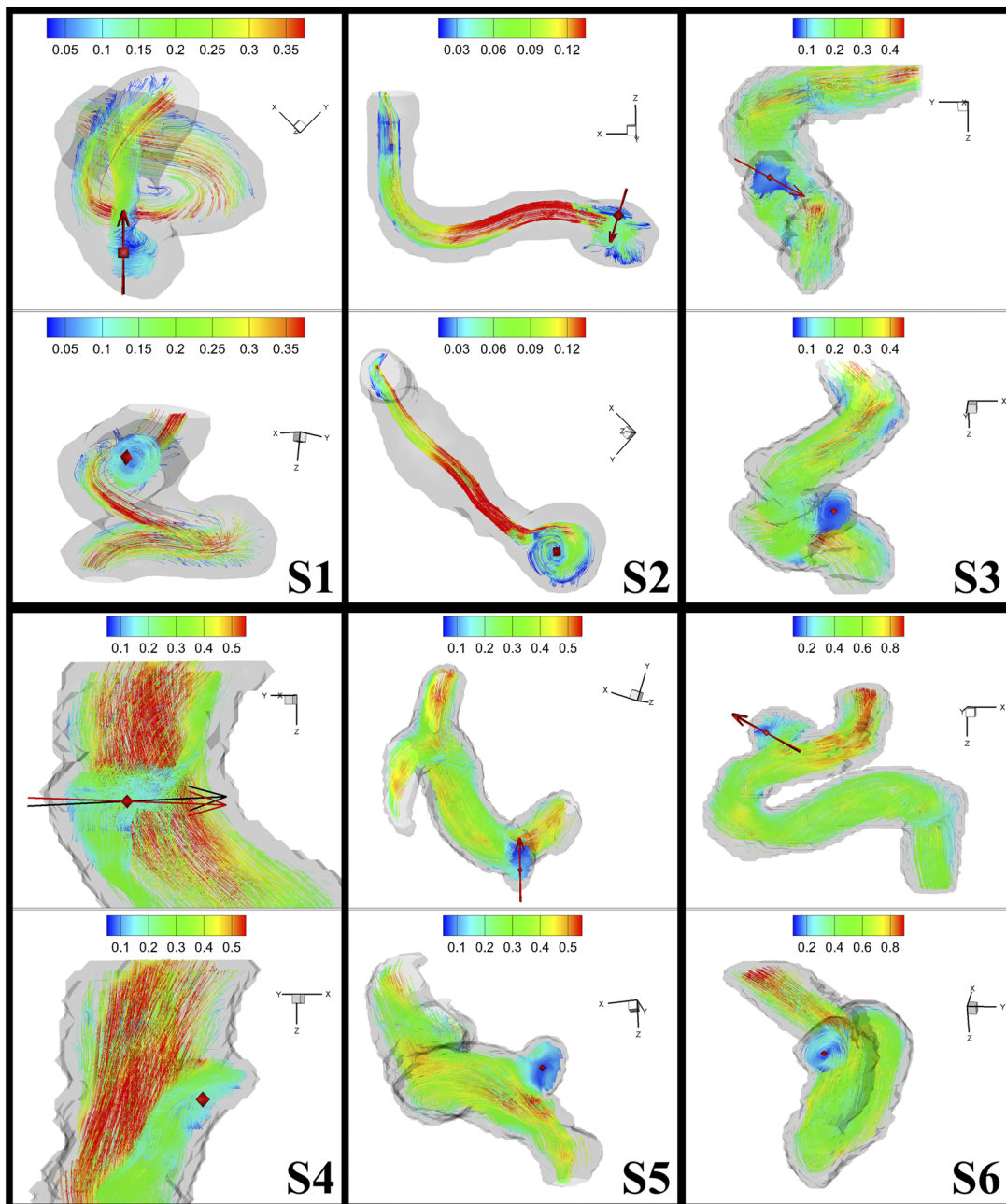


FIG. 3. Streamlines show the vortex motion pattern inside aneurysmal sac. Top: two spatially averaged vectors \vec{V}_{F_2} (black arrow) and \vec{V}_{ω} (red arrow). Bottom: vortex centers C_{F_2} and C_{ω} denoted by red diamonds.

the planar velocity vectors on the plane in CS_{F_2} (first column) and CS_{ω} (second column). Both C_{F_2} and C_{ω} have the maximum magnitude of this component of \vec{F}_{1,F_2} and $\vec{F}_{1,\omega}$, respectively, among all points contained in the plane. It can be seen that the planar velocity

vectors rotate around C_{F_2} or C_{ω} . The third column of Fig. 4 shows the scatter plots of the magnitude of this component of \vec{F}_{1,F_2} based on the \vec{V}_{F_2} vector against this component of $\vec{F}_{1,\omega}$ based on the \vec{V}_{ω} vector for each subject (linear regression fit slope: mean

TABLE III. Second column: $\theta_{\vec{T}_2, \vec{\omega}}$ between $\vec{V}_{\vec{T}_2}$ and $\vec{V}_{\vec{\omega}}$ for each subject. Third column: voxelwise averaged angle $\overline{\theta_{\vec{T}_2, \vec{\omega}}}$ between \vec{T}_2 and $\vec{\omega}$ at each voxel in the overlapping part of the defined high $\Gamma_{2, \text{magnitude}}$ and high Ω regions. Fourth column: kinetic energy ratio of the concentration on the plane perpendicular to $\vec{V}_{\vec{T}_2}$ to the total inside the defined high $\Gamma_{2, \text{magnitude}}$ region. Fifth column: kinetic energy ratio of the concentration on the plane perpendicular to $\vec{V}_{\vec{\omega}}$ to the total inside the defined high Ω region.

	$\theta_{\vec{T}_2, \vec{\omega}}$	$\overline{\theta_{\vec{T}_2, \vec{\omega}}}$	Ratio KE $_{\vec{T}_2}$	Ratio KE $_{\vec{\omega}}$
S1	4.41	7.51	0.81	0.83
S2	9.15	8.16	0.93	0.96
S3	1.17	4.98	0.92	0.94
S4	7.77	5.97	0.81	0.82
S5	2.77	5.89	0.93	0.93
S6	2.45	6.89	0.92	0.89

\pm std; min, max = 0.99 ± 0.02 , 1.01, 0.95). A small difference can be observed in the magnitude of this component of \vec{T}_1 between the two approaches, resulting from the small $\theta_{\vec{T}_2, \vec{\omega}}$ between $\vec{V}_{\vec{T}_2}$ and $\vec{V}_{\vec{\omega}}$.

III. DISCUSSION

In this work, we propose an approach to represent the average intra-aneurysmal three-dimensional vortex blood flow motion for each cardiac cycle using a previously described parameter, $\Omega(\omega)$, as well as a novel parameter \vec{T}_2 . This representational scheme allows us to characterize the entirety of the rotational motion observed within each small aneurysm included in this study in an easily visualized manner. We believe that our approach is improved with respect to prior methods for depicting intra-aneurysmal vortices by eliminating user dependent 2D plane selection induced biases. Our approach also identifies the rotational center of the 3D blood flow vortex within the aneurysmal volume. Although the six aneurysms that were studied in this series differ in size, shape, and location with resultant variations in flow strength, a uniform nonlinear relationship between $\Gamma_{2, \text{magnitude}}$ and Ω was observed within every aneurysm. This similarity between the high $\Gamma_{2, \text{magnitude}}$ region and the high Ω region enables us to be confident that \vec{T}_2 is indeed able to accurately recognize the flow region with high vortex motion within each aneurysm and, subsequently, to quantify its intensity.

With respect to the kinetic energy associated with the vortex motion within the aneurysms, as shown in Table III, fairly high kinetic energy is found along a plane oriented orthogonal to $\vec{V}_{\vec{T}_2}$ or $\vec{V}_{\vec{\omega}}$, in contrast to the lower KE values found along $\vec{V}_{\vec{T}_2}$ or $\vec{V}_{\vec{\omega}}$. Nevertheless, the lower KE values found along $\vec{V}_{\vec{T}_2}$ or $\vec{V}_{\vec{\omega}}$ propel the vortical flow to rotate forward and evolve out of the aneurysmal sac. In each aneurysm, the KE ratios derived from \vec{T}_2 and from $\Omega(\omega)$ are slightly different from each other due to the existence of the discrepancy in $\vec{V}_{\vec{T}_2}$ and $\vec{V}_{\vec{\omega}}$ directions, respectively. This discrepancy could reflect the differences in the physical mechanisms, which underlie \vec{T}_2 and $\Omega(\omega)$. \vec{T}_2 defines the vortex motion in a manner similar to the rotational motion of rigid bodies around a center, without

taking deformation into account. However, the $\Omega(\omega)$ measure regards fluid particles as compliant and therefore incorporates pure shearing and irrotational deformational effects along with rotational motion. Therefore, the measured angle $\theta_{\vec{T}_2, \vec{\omega}}$ likely reflects the extent to which blood particles are deformed and sheared within the aneurysmal sac, an important variable where propagating the aneurysm and parent vessel walls could result in the activation of inflammatory processes, which have been shown to play a role in IA growth and rupture. Interestingly, despite the variations between these six small IAs in terms of shape, size, and anatomical location, $\theta_{\vec{T}_2, \vec{\omega}}$ did not vary very widely between subjects, and the maximum $\theta_{\vec{T}_2, \vec{\omega}}$ was below 10° , which is not large, suggesting that the relative contribution of shear and deformational effects within small IAs to global flow dynamics is still not large. This observation is supported by the small voxelwise averaged angle $\overline{\theta_{\vec{T}_2, \vec{\omega}}}$ between \vec{T}_2 and $\vec{\omega}$ over the overlapping part of the defined high $\Gamma_{2, \text{magnitude}}$ and high Ω regions, which is below 9° throughout subjects.

Our results are also noteworthy for the observation that although there exists a difference between two averaged vectors $\vec{V}_{\vec{T}_2}$ and $\vec{V}_{\vec{\omega}}$, the center of vortex motion for both measures was the same, denoting that the effects of shear and deformation are negligible within the center of the vortex. However, the average magnitude of shear and deformation tends to increase with an increase in the distance from the center of the vortex (given the fixed angle between $\vec{V}_{\vec{T}_2}$ and $\vec{V}_{\vec{\omega}}$). Large values for deformation and shear of fluid particles (from vortical flow) could occur in regions that are close to walls of the aneurysm if the aneurysm wall falls within the 3D region with high Ω values. Whether this phenomenon contributes to increased rupture rates found with large aneurysms (wherein larger absolute differences between deformational/shear and rotational flow are bound to be found near the walls) is an open question. Likewise, the relationship between wall shear stress (WSS) values close to the walls of the aneurysms and the distance between various segments of the aneurysm wall and the vortex center could also be worth investigating.

Our present study does suffer from several limitations. First of all, in this initial series, we included a limited number of subjects. We did not attempt to classify the aneurysms based on their shapes, even though the morphology of aneurysms has been known to influence the hemodynamic characteristics. This study was focused on developing and demonstrating an effective approach to directly identify the three-dimensional vortex motion, alleviating the need for manually defining 2D planes commonly used for vortex analysis, which can help accelerate data analysis while limiting users' induced biases. Our approach is also expected to indirectly reflect the deformation of the blood particles in small intracranial aneurysms regardless of their size and shape. The similarity reported here between results obtained with our proposed approach and other methods in a small group of patients gives us confidence that our methods can reliably visualize and characterize vortices in small aneurysms in a non-invasive manner using 4D Flow MRI scanning at 7 T despite the very limited aneurysm size (≤ 7 mm). Expanding such investigation to large longitudinal cohorts of patients will be necessary to determine whether the occurrence of aneurysm instabilities (e.g., aneurysm growth) known for their associations with higher aneurysm rupture risk could translate into deviations between the results of traditional

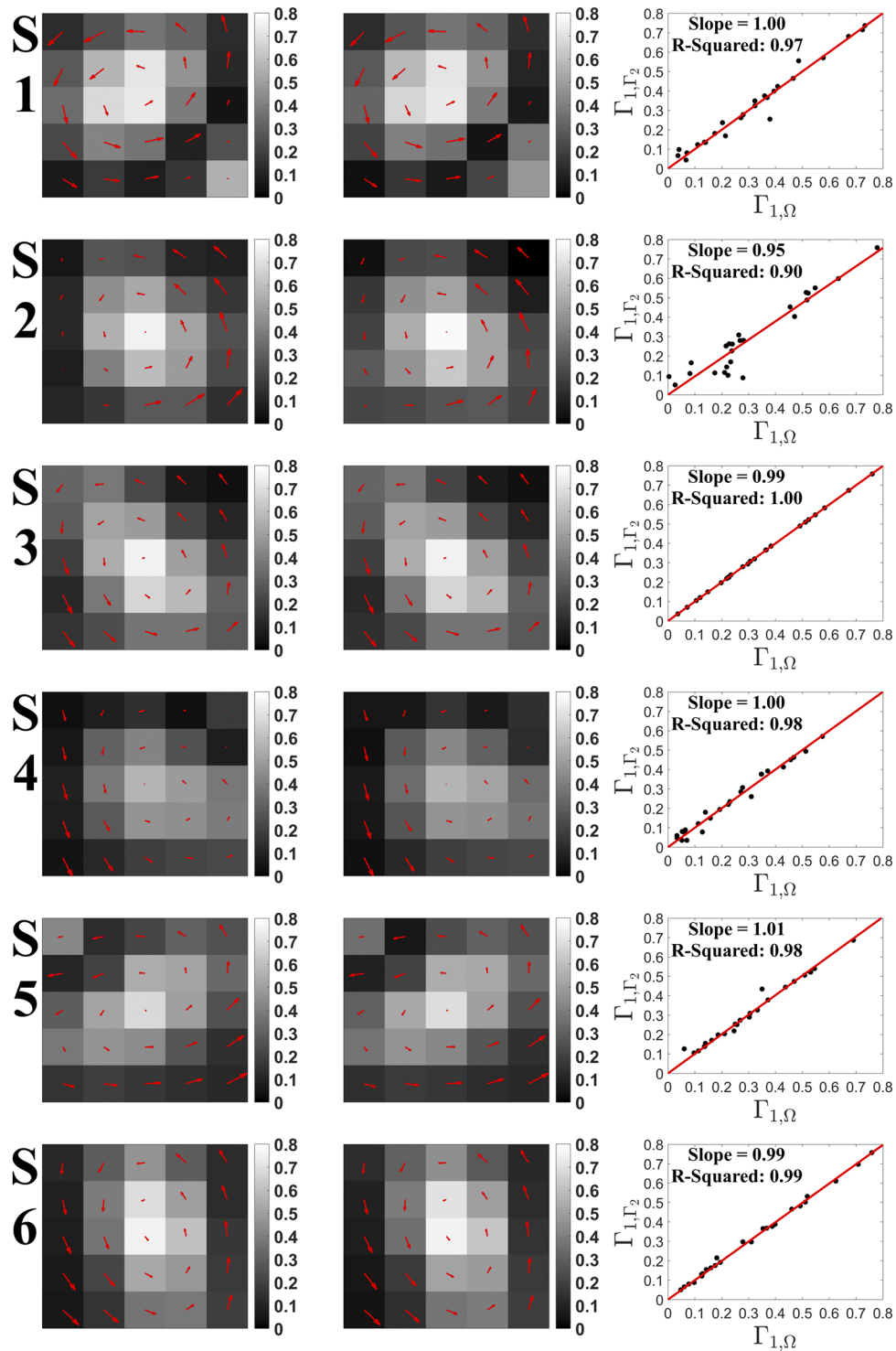


FIG. 4. Resampled plane perpendicular to the spatially averaged vectors \vec{V}_{I_2} (first column) and $\vec{V}_{\vec{\omega}}$ (second column) centered by C_{I_2} and $C_{\vec{\omega}}$. Color bars denote the magnitude of the component of $\vec{\Gamma}_{1,I_2}$ or $\vec{\Gamma}_{1,\vec{\omega}}$ in the same direction as \vec{V}_{I_2} or $\vec{V}_{\vec{\omega}}$. Red arrows show the planar velocity vectors. Third column: scatter plot of the magnitude of the component of $\vec{\Gamma}_{1,I_2}$ in the same direction as \vec{V}_{I_2} vs the magnitude of the component of $\vec{\Gamma}_{1,\vec{\omega}}$ in the same direction as $\vec{V}_{\vec{\omega}}$.

23 April 2024 20:49:43

methods vs our proposed approach (expected to be sensitive vs insensitive, respectively, to high shear and irrotational deformation). Recent advances providing faster MRI acquisition²⁴ capabilities will help broaden the scope of such studies. Comparing these experimental studies with computational fluid dynamic approaches²⁵ will further advance our understanding of aneurysm physiopathology.

IV. CONCLUSIONS

We present a novel approach to characterize the three-dimensional vortex motion inside patient specific ≤ 7 mm small intracranial aneurysmal sacs based on \vec{T}_2 and Ω ($\vec{\omega}$) based on 4D Flow MRI data. The magnitude of the newly extended three-dimensional vector \vec{T}_2 is effective in defining the high vortex motion region comparable to the existing dimensionless scalar Ω . Both the small angle, $\theta_{\vec{T}_2, \vec{\omega}}$, observed between the spatially averaged $\vec{V}_{\vec{T}_2}$ and $\vec{V}_{\vec{\omega}}$ vectors and the same located vortex motion center by \vec{T}_1 with \vec{T}_2 or Ω ($\vec{\omega}$) are consistent with a stable hemodynamic environments, with low shearing and irrotational deformation of the blood flow particles, for the small number of patients included in this pilot study.

ACKNOWLEDGMENTS

This work was supported by the National Institutes of Health (Grant Nos. P41 EB027061 and P30 NS076408).

Following informed consent, participants with IAs were enrolled in a prospective HIPAA compliant study approved by the Institutional Review Board (clinicaltrials.gov NCT02576743) of the University of Minnesota.

AUTHOR DECLARATIONS

Conflict of Interest

The authors have no conflicts to disclose.

DATA AVAILABILITY

The data that support the findings of this study are available from the corresponding author upon reasonable request.

REFERENCES

¹M. W. Vernooij, M. A. Ikram, H. L. Tanghe, A. J. P. E. Vincent, A. Hofman, G. P. Krestin, W. J. Niessen, M. M. B. Breteler, and A. Van Der Lugt, *N. Engl. J. Med.* **357**, 1821 (2007).

²K. Aishima, T. Shimizu, M. Aihara, and Y. Yoshimoto, *World Neurosurg.* **95**, 434 (2016).

³D. M. Panczykowski, C. Veet, N. Parekh, and S. L. Blackburn, *Neurosurgery* **66**, nyz310_302 (2019).

⁴M. Korja and J. Kaprio, *Nat. Rev. Neurol.* **12**, 50 (2016).

⁵M. Zanaty, B. Daou, N. Chalouhi, R. M. Starke, P. Jabbour, and D. Hasan, *J. Am. Heart Assoc.* **5**, e003936 (2016).

⁶D. J. Nieuwkamp, L. E. Setz, A. Algra, F. H. Linn, N. K. de Rooij, and G. J. Rinkel, *Lancet Neurol.* **8**, 635 (2009).

⁷A. Falk Delgado, T. Andersson, and A. Falk Delgado, *J. NeuroInterventional Surg.* **9**, 264 (2017).

⁸H. Isoda, Y. Ohkura, T. Kosugi, M. Hirano, H. Takeda, H. Hiramatsu, S. Yamashita, Y. Takehara, M. T. Alley, R. Bammer, N. J. Pelc, H. Namba, and H. Sakahara, *Neuroradiology* **52**, 921 (2010).

⁹S. Schnell, S. A. Ansari, P. Vakil, M. Wasielewski, M. L. Carr, M. C. Hurley, B. R. Bendok, H. Batjer, T. J. Carroll, J. Carr, and M. Markl, *J. Magn. Reson. Imaging* **39**, 120 (2014).

¹⁰K. Futami, T. Kitabayashi, H. Sano, K. Misaki, N. Uchiyama, F. Ueda, and M. Nakada, *Am. J. Neuroradiol.* **37**, 1318 (2016).

¹¹J. R. Cebal, F. Mut, J. Weir, and C. M. Putman, *Am. J. Neuroradiol.* **32**, 264 (2011).

¹²J. R. Cebal, F. Mut, J. Weir, and C. M. Putman, *Am. J. Neuroradiol.* **32**, 145 (2011).

¹³A. Zhou, O. Amili, S. Moen, M. Toloui, A. W. Grande, F. Coletti, B. Jagadeesan, and P.-F. Van de Moortele, in *Proceedings of 27th International Society of Magnetic Resonance in Medicine Annual Meeting and Exhibition in Montréal Canada* (ISMRM, 2019), p. 1989; available at <https://archive.ismrm.org/2019/1989.html>.

¹⁴K. Futami, T. Uno, K. Misaki, S. Tamai, I. Nambu, N. Uchiyama, and M. Nakada, *Am. J. Neuroradiol.* **40**, 2111 (2019).

¹⁵K. Futami, I. Nambu, T. Kitabayashi, H. Sano, K. Misaki, N. Uchiyama, and M. Nakada, *Neuroradiology* **59**, 411 (2017).

¹⁶J. -Z. Wu, H. -Y. Ma, and M. -D. Zhou, *Vorticity and Vortex Dynamics*, (Springer Science+Business Media, 2007).

¹⁷S. Tateshima, K. Tanishita, H. Omura, J. P. Villablanca, and F. Vinuela, *Am. J. Neuroradiol.* **28**(4), 622–627 (2007); available at <http://www.ajnr.org/content/28/4/622>.

¹⁸C. J. World, G. Garin, and B. C. Berk, *Curr. Atheroscler. Rep.* **8**, 240 (2006).

¹⁹N. F. Jufri, A. Mohamedali, A. Avolio, and M. S. Baker, *Vasc. Cell* **7**, 8 (2015).

²⁰M. Markl, A. Harloff, T. A. Bley, M. Zaitsev, B. Jung, E. Weigang, M. Langer, J. Hennig, and A. Frydrychowicz, *J. Magn. Reson. Imaging* **25**, 824 (2007).

²¹L. Graftieux, M. Michard, and G. Nathalie, *Meas. Sci. Technol.* **12**, 1422 (2001).

²²C. Q. Liu, Y. Q. Wang, Y. Yang, and Z. W. Duan, *Sci. China Phys., Mech. Astron.* **59**, 684711 (2016).

²³C. Liu, Y.-s. Gao, X.-r. Dong, Y.-q. Wang, J.-m. Liu, Y.-n. Zhang, X.-s. Cai, and N. Gui, *J. Hydrodyn.* **31**, 205 (2019).

²⁴L. M. Gottwald, J. Töger, K. Markenroth Bloch, E. S. Peper, B. F. Coolen, G. J. Strijkers, P. Van Ooij, and A. J. Nederveen, *Am. J. Neuroradiol.* **41**, 1201 (2020).

²⁵M. Meuschke, S. Oeltze-Jafra, O. Beuing, B. Preim, and K. Lawonn, *IEEE Trans. Visualization Comput. Graphics* **25**, 2404 (2019).